Radar Scattering from Special Media in the MST Regime: Meteors, Hydrometeors, Lightning, and Dusty/Icy Plasma

JOHN Y. N. CHO

Department of Earth, Atmospheric, and Planetary Sciences

Massachusetts Institute of Technology

Cambridge, Massachusetts

U. S. A.

Radar scattering from special media in the MST Regime: Meteors, Hydrometeors, Lightning, and Dusty/Icy Plasma

Mesosphere-stratosphere-troposphere (MST) radars generally operate in VHF and UHF bands and are used to observe the scattering of radio waves from clear-air refractive-index fluctuations. Although not necessarily optimized for detecting other types of scatterers, the signals they receive nevertheless contain non-clear-air echoes, which may be cursed as contaminations of the desired data. For example, radar scatter from rain and lightning during a deep convective storm might dominate the Doppler spectra from which one is trying to extract high-resolution wind-vectors. Or meteor echoes may disrupt one's measurement of mesospheric turbulent layers. But, as the old adage states, one's noise is another's signal. In some cases the particular properties of an MST radar can be used advantageously to study phenomena for which it was not designed. The purpose of this lecture is to introduce these special scattering media and to present ways in which MST radars can contribute to their study. The media covered will be (1) Clouds and precipitation, (2) transient plasma: lightning and meteors, (3) dusty/icy plasma: polar mesosphere summer echoes (PMSE), and (4) F-region plasma: equatorial spread F (ESF). (Although the last topic is above the mesosphere, we include it because the Indian NMRF can be used to study it.) To place the MST radar in context to the other types of radar used specially for these media (like weather radars and meteor radars), I will also provide a brief historical account in each section. As this is not a technical review paper I will not provide a comprehensive set of references. Instead citations will be used for examples and as sources for more complete coverage of the topics. Good background material for sections 1 and 2 can be found in the following books: *Radar in Meteorology* [2], *Doppler Radar and Weather Observations* [15], *and Meteor Science and Engineering* [41].

1. Scattering From Clouds and Precipitation

The weather radar was a wartime baby, born during the intense and secret development of aircraft detection systems by the Allies in the 1940s. Even before the outbreak of WWII, both sides had adopted radars for military use, but it was the British invention of the cavity magnetron (providing superior sensitivity, resolution, and portability by extending the operational frequency from UHF up to the S and X bands) that proved decisive in the struggle for air supremacy. But the move to shorter wavelengths also made the radars more sensitive to environmental "noise" such as precipitation, insects, and birds. At first these extra signals were investigated as nuisances, but as long-range night- time bombing missions became more common and crucial in the latter stages of the war, the concept of using the sweeping radars for weather disturbance detection was born. (Figure 1 displays a radar scope image of a different kind of cloud [53]).

1.1 Brag Versus Rayleigh scatter

Radio waves scatter from discontinuities in the refractive index of the propagation medium. For a diffuse medium like clear air, the radio wave scatters from refractive index changes that match the Bragg condition,

$$\kappa = \kappa_i - \kappa_s \tag{1}$$

Where κ_i (rad/m) is the incident wavenumber vector, κ_s (rad/m) is the scattered wavenumber vector, and κ (rad/m) is the wavenumber vector of the refractive index perturbation that fulfills the Bragg condition. For backscatter $\kappa_s = -\kappa_i$, so $\kappa = 2\kappa_i$. In other words, backscatter systems "see" refractive index structures at half the radar wavelength.

Statistically, in the neutral atmosphere the energy in the refractive index fluctuations goes up with the length scale. This is true regardless of weather the fluctuations are generated by turbulence or some other mechanism. Therefore, the Bragg scattering cross section is generally larger for longer wavelength radars. Other considerations such as resolution and cost put an upper limit to the practical radar wavelength for clear-air applications. This is why MST radars have mostly been built in the VHF range - it is a good compromise between all the driving factors.

However, if macroscopic particles are present inside the radar volume, then the radio wave will be scattered by them according to the Rayleigh approximation.

$$\sigma_i = \frac{\pi^5 |K_i|^2 D_i^6}{\lambda^4} \tag{2}$$

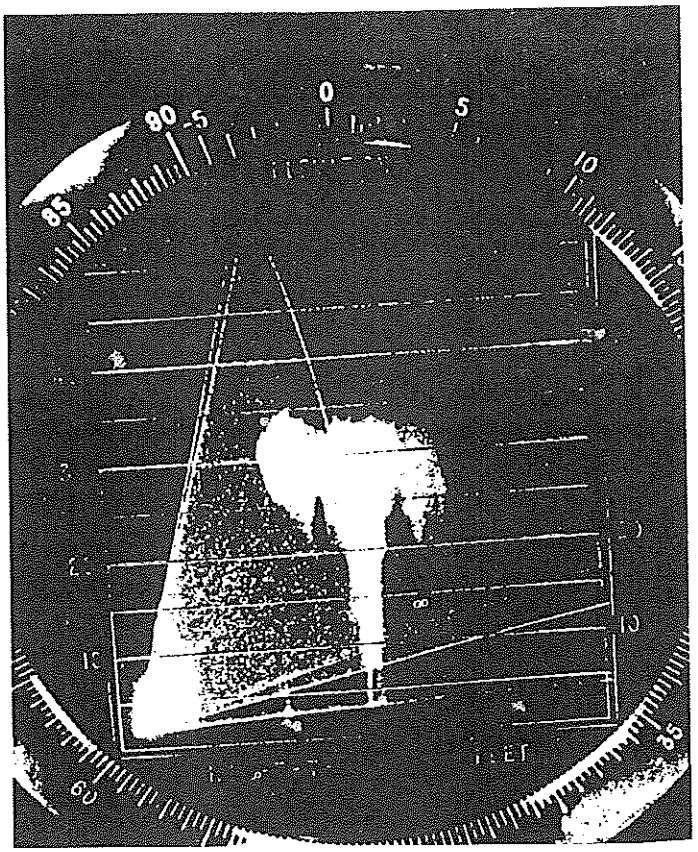

Figure 1: A mushroom cloud from a nuclear test explosion in the Marshall Islands as observed with a weather radar.

where σ_i (m^2) is the backscatter cross section for a single spherical drop, D_i (m) is the diameter of each particle, λ (m) is the radar wavelength, and $K_i = (m^2 - 1)/(m^2 + 2)$ with m as the complex refractive index of the particle. We immediately see that Rayleigh scattering increases with decreasing radar wavelength. This is why weather radars use much higher frequencies than MST radars. $|K|^2 \sim 1$ for water and $|K|^2 \sim 0.2$ for ice. Mixtures of water and ice, such as water-coated ice, or spongy/fluffy ice can have different values of $|K|^2$ (see, e.g., [4]). The Rayleigh approximation is valid for $D \leq \lambda/16$, so it is always correct for atmospheric droplets observed by VHF and UHF radars. For higher frequency systems Mie scattering starts to take over for the largest particles. Departure of the drop shape away from a sphere will also affect the properties of radio-wave scattering, in particular the wave polarization. This effect is used by dual-polarization radars to discriminate between different types of hydrometeors (see Chapter 8 in reference [15]).

The radar reflectivity per unit volume (m^{-1}) is given by

$$\eta = \frac{\sum_i \sigma_i}{V} \tag{3}$$

where V (m^3) is the radar volume. So for a size distribution of droplets across M bins,

$$\eta = \frac{\pi^5}{\lambda^4} \sum_{i=1}^{M} N_i |K_i|^2 D_i^6 \tag{4}$$

where N_i (m^{-3}) is the particle number density for each diameter. Here we made the assumption that K is constant for a given drop size. In operational meteorology the further assumption of K constant for all particle sizes is made to arrive at the equation

$$\eta = 10^{-18} \frac{\pi^5}{\lambda^4} |K|^2 Z \tag{5}$$

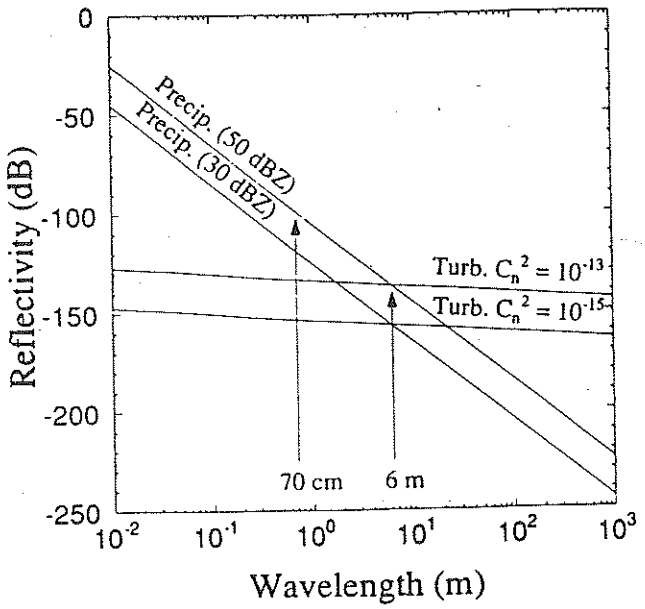

Figure 2: Plot of η vs. λ for precipitation and clear-air turbulence. The values of Z (dBZ) and C_n^2 shown are typical of those found in a thunderstorm environment. The wavelengths 70 cm and 6 m correspond to those of the UHF and VHF radars at the Arecibo Observatory.

where

$$Z \equiv \sum_{i=1}^{M} N_i D_i^6 \tag{6}$$

($\mathrm{mm}^6\ \mathrm{m}^{-3}$) is called the radar reflectivity factor.

Going back to the case of Bragg scatter, in particular for turbulent scatter we have a volume reflectivity of

$$\eta = 0.38\lambda^{-\frac{1}{3}} C_n^2 \tag{7}$$

where C_n^2 ($\mathrm{m}^{-2/3}$) is the turbulence structure constant that characterizes the strength of refractive index fluctuations (see, e.g., [24]). The particular niche for VHF MST radars in cloud/precipitation studies lies in the fact that they can detect both Bragg scatter from the air and Rayleigh scatter from precipitation. Figure 2 shows the range of typical η for both Rayleigh scatter from hydrometeors and clear-air turbulent scatter during a thunderstorm [30]. Note that a 50-MHz radar (λ = 6 m) is in a position to detect both types of scatter, whereas radars at higher frequencies will generally only observe the precipitation. (The presentation in Figure 2 is somewhat deceptive in that C_n^2 itself is actually strongly dependent on λ. As mentioned earlier, η for clear-air turbulent scatter goes up with λ. Therefore, holding C_n^2 constant over λ is not realistic. An example of simultaneous observation of clear-air and precipitation echoes is shown in Figure 3 [26].

But why is the simultaneous observation of clear-air and precipitation echoes important? We answer this question in the next section.

1.2 Estimating Drop-Size Distribution and Precipitation Rate

Ever since the first detection of hydrometeors by radar (nearly simultaneously in England and in Cambridge, Massachusetts), one of the holy grails for radar meteorologists has been the determination of rainfall rate. Before the advent of the Doppler and dual-polarization radars, reflectivity was the only information available from which to base a rainfall estimate. Thus, in simple fashion an empirical relationship was established between the two quantities of the form

$$Z = aR^b \tag{8}$$

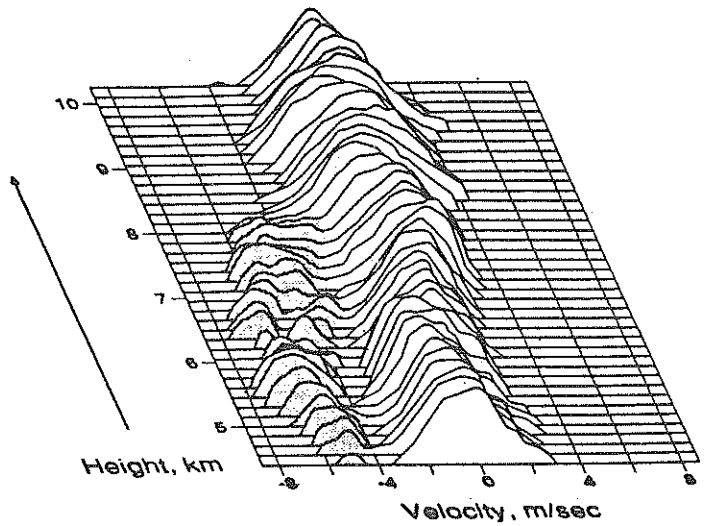

Figure 3: Vertical incidence Doppler spectra from the VHF radar at the Arecibo Observatory, illustrating the separation of returns associated with air motions (unshaded) from those due to precipitation (gray shading).

where R (mm/h) is the precipitation rate. Commonly used values for a and b are $a = 200$ and $b = 1.6$ for stratiform rain, known as the Marshall-Palmer formula [35]. It is clear, however, from (6) that this relation depends critically on the drop size distribution (DSD). Marshall and Palmer fitted exponentials to their observed DSD to arrive at their formula. However, because actual DSDs vary widely depending on location, type of rainstorm, and season a more general gamma distribution has been proposed [56]

$$N = N_0 D^{\mu} e^{-\Lambda D} \tag{9}$$

where N_0 ($\mathrm{m}^{-3}/\mathrm{mm}$), μ, and Λ (m^{-1}) are determined empirically for different types of precipitation. Examples of observed DSDs are shown in Figure 4 [31]. These early determinations of DSDs were conducted in situ with, for example, filter paper at ground level. The development of Doppler radars, though, made it possible to estimate the DSDs remotely and in real time by making use of the relationship between drop size and velocity. A commonly used empirical equation for water droplet terminal velocity (m/s) is [22, 5]

$$w_t = \left(\frac{\rho_0}{\rho}\right)^{0.45} (-9.65 + 10.3\, e^{-600D}) \tag{10}$$

which fits the observed values well in the range $D = 6 \times 10^{-4}$ to 5.8×10^{-3} m; ρ (kg m^{-3}) is the density of the ambient air and ρ_0 (kg m^{-3}) is the density of air at a pressure of 760 mm Hg and a temperature of 20°C. Note that for $D < 0.1$ mm the fall speed is upward and therefore (10) is definitely not valid in this size range.

For solid ice spheres, the terminal velocity is given by

$$w_t = \left(\frac{4\rho_i g D}{3\rho C_d}\right)^{\frac{1}{2}} \tag{11}$$

where ρ_i (kg m^{-3}) is the density of ice, $g = 9.8$ m s^{-2} is the gravitational acceleration, and C_d is the drag coefficient. Experiments show C_d to be between about 0.82 and 0.97 for hailstones with diameters less than 25 mm [38].

We now have almost enough information to extract DSDs (and thus a more accurate precipitation rate) from radar vertical Doppler velocity spectra. However, there are still two factors that we need to take care of. The first is that the terminal velocity is the relative velocity between the droplet and the ambient air, whereas the radar Doppler velocity of precipitation is the velocity with respect to the Earth's surface.

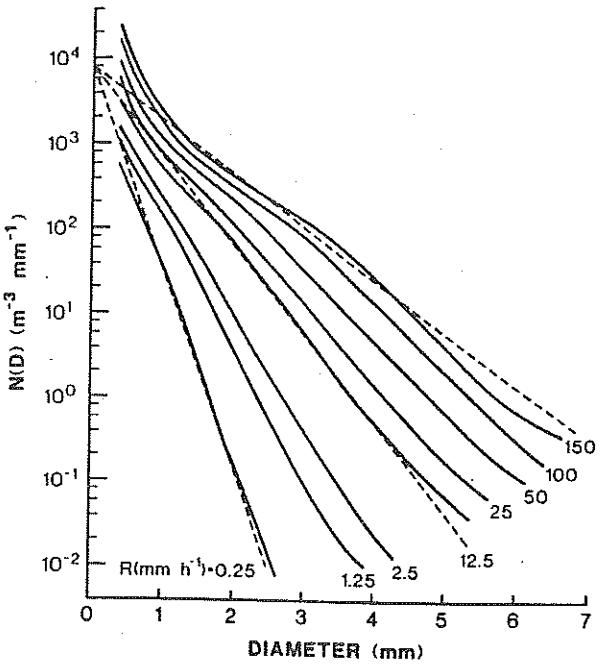

Figure 4: Example of measured raindrop-size distributions for various rainfall rates. Dashed lines are selected comparisons with the Marshall and Palmer observations.

Therefore, we need to know what the vertical air motion is. This is where a VHF radar comes in handy as seen earlier—it can simultaneously measure the air motion and remove that velocity component from the precipitation spectra (Figure 3).

Secondly, the precipitation spectra are distorted by the presence of turbulence. Again, VHF radars can help deconvolve this effect by being able to measure the clear-air turbulence spectra.

Now we can put together all the pieces to outline a method for an estimation of precipitation rate. Much of the following is taken from Wakasugi *et al* [62, 63].

The normalized vertical Doppler velocity spectrum of precipitation scatter is related to the DSD by

$$S_p(w)\,dw = \frac{D^6 N(D)}{Z}\,dD \tag{12}$$

where (10) or (11) can be used depending on the assumption of either water or ice particles to get dD/dw. For turbulence, the normalized Doppler spectrum is fairly well approximated by a Gaussian

$$S_t(w) = (2\pi\sigma_w^2)^{-\frac{1}{2}} e^{-\frac{w^2}{2\sigma_w^2}} \tag{13}$$

where σ_w (m/s) is the spectral width parameter. A note of caution must be inserted here. The Doppler spectral width measured by a vertically pointing radar, especially one with a broad antenna beam, will have not only a turbulent component but also a significant cross-wind widening component known as beam broadening. One should remove this non-turbulent spectral width by making use of the observed horizontal velocities [24].

If we assume that particles of all sizes are advected according to the turbulent motions, then the Rayleigh-scatter spectrum will be distorted by turbulence, which can be expressed mathematically as a convolution. Also, we need to take into account that the Doppler spectrum will be shifted by the vertical velocity $\bar{w}$ of the ambient air. Thus, the sum spectrum of clear-air and precipitation scatter can be written as

$$S(w) = P_p S_p(w - \bar{w}) * S_t(w) + P_t S_t(w - \bar{w}) \tag{14}$$

where P_p and P_t are the peak echo powers for the precipitation and clear-air scattering, and $*$ denotes a convolution.

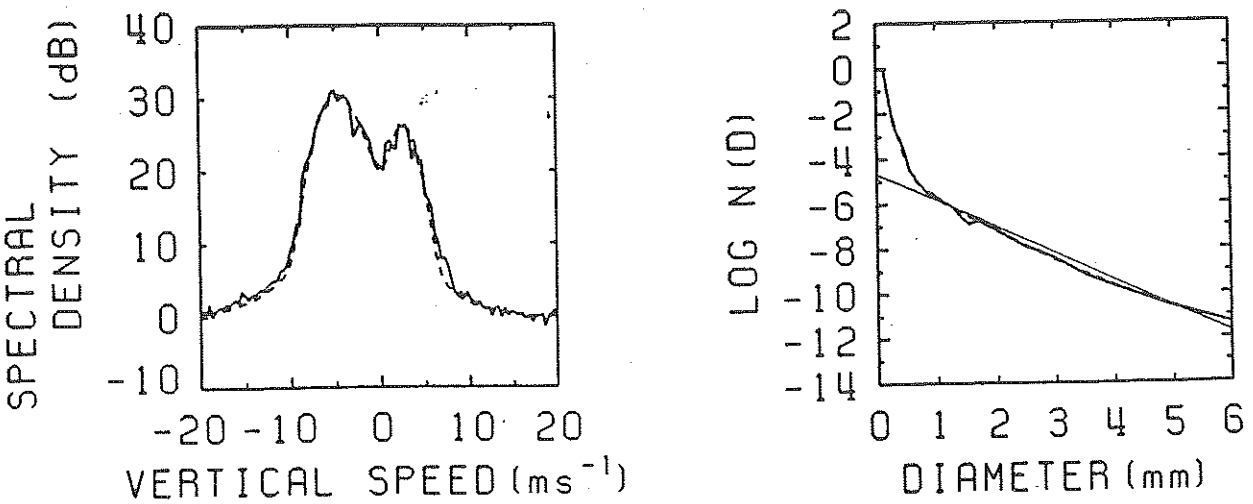

Figure 5: (Left) An example of a 1-minute averaged vertical Doppler spectrum (solid) and the fitted spectrum (dashed). The spectral density is relative intensity and positive motion is upward. (Right) The DSD is given by the solid curve and its fitted curve by the dashed line. They lie on top of each other and are not distinguishable. These curves include the broadening effects due to turbulence and data truncation. The linear line corresponds to an exponential distribution $N_0 e^{-\Lambda D}$ using the extracted parameters $N_0 = 2.3 \times 10^{-5}$ mm^{-4} and $\Lambda = 2.73$ mm^{-1}. Data were sampled on 25 June 1985 at 2.4 km altitude.

Finally, since the calculated spectrum from sampled data must be truncated according to some window function, we need to take this into account when making the comparison between theory and data. So the observed normalized spectrum, S_o, will be (14) convolved with the window function W to get

$$S_o(w) = [P_p S_p(w - \bar{w}) * S_t(w) + P_t S_t(w - \bar{w})] * W(w) \tag{15}$$

A nonlinear least-squares fit to the observed spectrum then yields the desired parameters. Figure 5 (left) shows the result of such a fitting. The panel on the right displays the derived DSD (which still includes the turbulence and data truncation broadening effects).

Let us now convert the DSD to an estimate of the precipitation rate. The number of drops $N_a(D)$ for diameter between D and $D + dD$ falling on area dA in time dt is

$$\frac{N_a(D)\,dD}{dA\,dt} = N(D) w_t(D)\,dD \tag{16}$$

Assuming spherical shapes, each drop has a water mass m_w (kg) of

$$m_w(D) = \frac{\pi}{6} \rho_w D^3 \tag{17}$$

where ρ_w (kg m^{-3}) is the density of liquid water/ice. So the total mass of water per unit area and time is

$$\frac{\int_0^\infty N_a(D) m_w(D)\,dD}{dA\,dt} = \frac{\pi \rho_w}{6} \int_0^\infty D^3 N(D) w_t(D)\,dD \tag{18}$$

For rain, then, the rainfall rate measured as depth of water per unit time (mm/h) is

$$R = 6 \times 10^5\, \pi \int_0^\infty D^3 N(D) w_t(D)\,dD \tag{19}$$

Comparing R as estimated from VHF radar data to that measured in situ on the ground is an ongoing research area. It is not yet an operationally proven technique. One problem for MST radars in estimating R is that one must make an assumption about the type of hydrometeors. If a dual-polarization weather radar is available for viewing the same volume as the VHF radar, then this ambiguity could be eliminated. Also

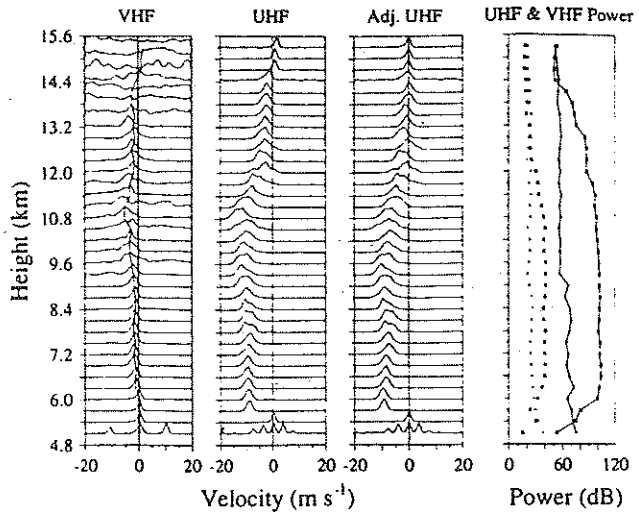

Figure 6: Doppler spectra from the Arecibo VHF and UHF radars. Here the VHF radar is only responding to the Bragg scatter, while the UHF is Rayleigh scattering. Thus, the VHF Doppler shifts are used to adjust the UHF spectra to their true terminal velocity spectra. In the power/noise profiles, the UHF values are given by asterisks and the VHF values by plus signs. The symbols connected by line segments denote power, whereas those not connected indicate noise level.

the assumption we made about turbulent motions advecting the droplets regardless of size is not necessarily a good approximation. Heavier particles are less likely to be affected by turbulent motions than lighter ones. VHF radars are also not sensitive to the smaller droplets; besides, if the terminal velocities are too small for the Rayleigh spectrum to be separated from the Bragg spectrum, then the procedure outlined above for extracting the DSD would not work. Therefore, it is ideal to have a higher frequency radar that can observe the same volume as the VHF radar. For example, the Arecibo Observatory has a co-linear VHF and UHF system, which makes it ideal for these purposes (Figure 6 [9]).

1.3 Scattering From Clouds

Although cloud droplets are too small to provide Rayleigh scattering for MST radars, the water vapor variations inside a cloud can enhance the refractive index fluctuations that generate Bragg scattering. The radio refractive index of air is given by

$$n = 10^6 \times \left(776\frac{P}{T} + 6000\frac{qP}{T^2}\right) + 1 \tag{20}$$

where P is pressure (kPa), T is temperature (K), and q is specific humidity (g/kg). The fluctuation in n is

$$\delta n = \frac{\partial n}{\partial T}\delta T + \frac{\partial n}{\partial q}\delta q + \frac{\partial n}{\partial P}\delta P \tag{21}$$

Because the fluctuations are statistically random, one looks at the ensemble average of the fluctuation power, $\langle \delta n^2 \rangle$. To get an idea of the relative importance of the different terms, one can plug in some representative values: $T = 280$ K, $P = 85$ kPa, and $q = 8$ g/kg to get [61]

$$\langle \delta n^2 \rangle \approx 10^{-12} \times \left(1.47 \langle \delta T^2 \rangle + 42.3 \langle \delta q^2 \rangle - 15.8 \langle \delta T\, \delta q \rangle\right) \tag{22}$$

where the terms with pressure fluctuations have been dropped because they are negligible. Note that if water vapor fluctuation is present, it contributes strongly to $\langle \delta n^2 \rangle$, even for "clear air" conditions. Also the radar echo power can either be enhanced or weakened depending on the sign of the correlation between δT and δq.

There is thus potential for MST radars to make contributions to the study of clouds, although this possibility has not been exploited much yet. There is still more work needed, both on the theoretical and observational fronts, to quantify the relationship between cloud dynamics and refractive index structuring.

In a totally different altitude regime, the upper mesosphere, ice clouds can form in the extremely low temperatures of the polar summer. They are known as noctilucent or polar mesospheric clouds. Because of the presence of plasma at these heights, the ice particles are thought to be electrically charged. By coupling the dynamics of the ice aerosols electrically to the free electrons, these clouds (or more likely their subvisible precursors) are believed to help generate the peculiarly strong radar scattering known as PMSE. This topic will be discussed in Section 3.

2 Scattering From Transient Plasma: Lightning and Meteors

Lightning and meteors are fascinating optical phenomena that have attracted people's interest since the dawn of consciousness. Although occurring in very different levels of the atmosphere, they share a certain basic characteristic: they are both short-lived plasma phenomena that occur in thin, elongated structures. Thus, their radar scattering characteristics have some things in common.

Because of the roots of radar in the study of the ionosphere, it was natural that meteoric effects would be noticed quickly. During the 1920s, a number of ionospheric investigators noticed transient enhancements in the nighttime E-region electron density. The idea that meteors were creating extra ionization were confirmed during the 1931 and 1932 Leonid showers [52, 49]. Since then, application of the radar meteor echo has ranged from long-range communication using forward scatter to estimation of the ambient wind and diffusion coefficient, not to mention the study of the ablating meteoroids themselves. Recently there has been a revival of interest in the basic physics of meteoric radar scatter with puzzling new observations coming from large-aperture radars. In this lecture we will focus on this aspect of meteoric radar studies.

Lightning echoes were first observed by 1.5-m [45] and 4-m [51] radars in 1943, within 2 years of the first thunderstorm observations with a microwave radar. Although interest in radar lightning studies has been on and off over the years, perhaps due to the lack of an applied side, new techniques such as interferometry, multi-frequency, and dual-polarization have helped to make forward progress in recent years. But again our emphasis here will be on lightning observations by MST systems.

2.1 Overdense Versus Underdense Plasma

When an electromagnetic wave impinges on a plasma, the manner in which the interaction takes place is critically dependent on the frequency of the wave versus the so-called plasma frequency (Hz)

$$f_p = \frac{1}{2\pi}\left(\frac{N_e e^2}{\epsilon_0 m_e}\right)^{\frac{1}{2}} \tag{23}$$

where N_e (m^{-3}) is the electron number density, $e = 1.6\times10^{-19}$ C is the electron charge, $\epsilon_0 = 8.85\times10^{-12}$ F/m is the free-space permittivity, and $m_e = 9.1\times10^{-31}$ kg is the electron mass. When the wave frequency is much below f_p, the electrons can respond in phase and help shield the plasma interior, thus reflecting the wave like a good conductor. This condition is called overdense. When the wave frequency is much above f_p, the electrons cannot respond in phase and the plasma behaves like a dielectric. This condition is called underdense. Note that because the plasma is imbedded in a neutral gas, it cannot behave as either a perfect conductor or a lossless dielectric. Therefore, the electron-neutral collision frequency is also an important parameter and must be included for an accurate computation of the complex refractive index.

If the source of ionization is thermal, then the air temperature is the driving factor behind the electron density, and thus the plasma frequency. Figure 7 shows calculations of f_p versus plasma temperature at 1 atm and 0.1 atm, which are suitable for the lightning regime [67]. Note that at 5000 K the f_p is above all frequencies used for meteorological radars, and at 3000 K f_p is above the frequencies used for MST radars. Since laboratory studies of electrical arcs and spectroscopic measurements of lightning indicate temperatures in excess of 5000 K, lightning plasma should always start out as overdense for weather and MST radars. Thus, underdense theories of lightning radar scatter that have been proposed in the past should be ruled out (although lightning plasma can become underdense in the latter stages of decay). Meteors, on the other hand, are believed to start out as both overdense and underdense for VHF and UHF radars, depending on the altitude, mass, and velocity of the meteor.

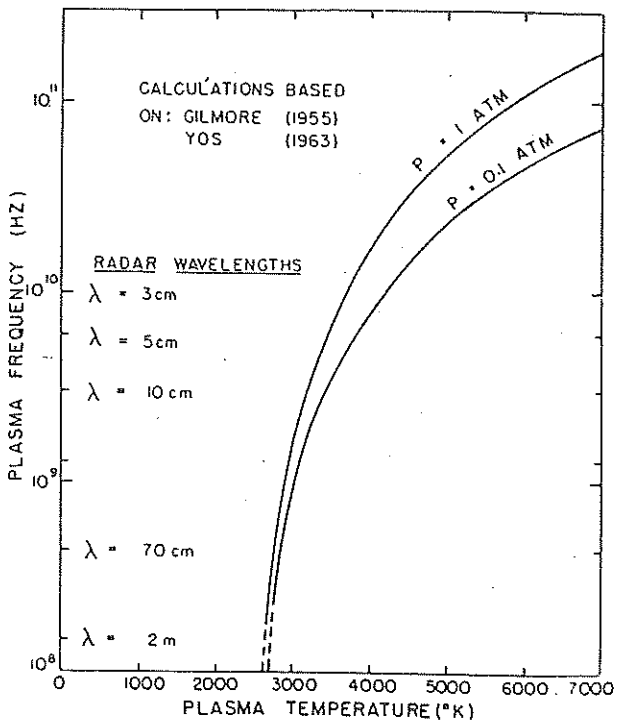

Figure 7: Plasma frequency versus temperature for hot air at two selected pressures.

2.2 Scattering From Lightning

Unlike the straight (at least initially) and single cylinder of ionization that a meteor leaves in its wake, lightning discharges form a complex dendritic structure with multiple tree-like branches. (For more information on lightning, see the books by Uman [57, 58]). The same type of branching structure is also observed at optical and radio wavelengths. Figure 8 shows lightning images taken from early photographs of a radar scope [32]. The radar scattering problem for lightning is therefore simple in that the medium is well approximated by a conductor that is long and thin with respect to the radar wavelength, but complex with respect to the geometry. Figure 9 shows the progression in complexity of the geometric models of lightning [67]. The simplest model, one long and thin wire, scatters extremely anisotropically. The assumption of random orientation (Figure 9b) for a collection of separate wire segments smooths out this anisotropy. A simple analytic result for this case is quoted by [67] to yield a radar cross section of

$$\sigma_a = \frac{3\pi\lambda L}{8\pi^2 + 32\left[\gamma + \log(\frac{\pi r}{\lambda})\right]^2} \tag{24}$$

where L (m) is the length of the wire segment, r (m) is the radius of the wire, and $\gamma = 0.57721$ is Euler's constant. The more realistic-looking models of Figure 9c and d cannot be handled analytically, and must be solved numerically. (Perhaps fractal models would be appropriate.) Some progress has been made towards numerical solutions [67], but a good representation of geometric features that span many orders of magnitude in length scale is a difficult scattering problem to compute.

The obvious advantage of using radio frequencies to study lightning is that there are many lightning events hidden from optical view by thick clouds. In fact, from a cloud microphysics point of view, these are the most interesting types of lightning, because they are directly the result of electrical charge separation within the cloud. However, precipitation inside a cloud can obscure even radar "visibility" of lightning by producing high reflectivity in Doppler velocity bins in the same range as the lightning echo. This is where a VHF radar has an advantage over higher-frequency weather radars, because of its lower sensitivity to Rayleigh scattering from precipitation and a larger cross section for lightning scatter.

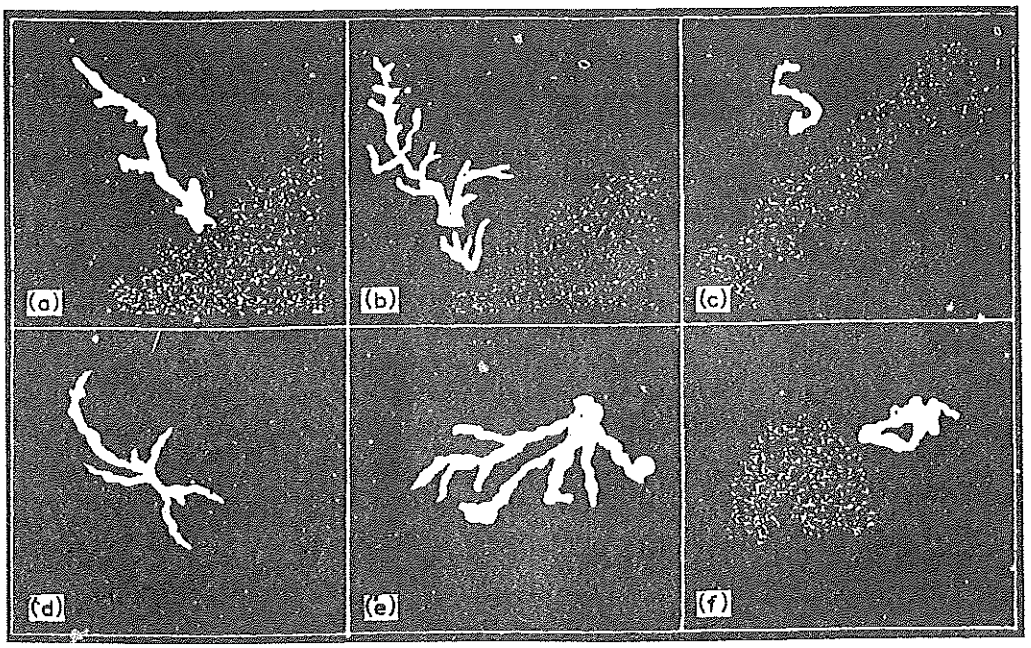

Figure 8: Basic types of lightning echo images drawn from photographs of a radar scope.

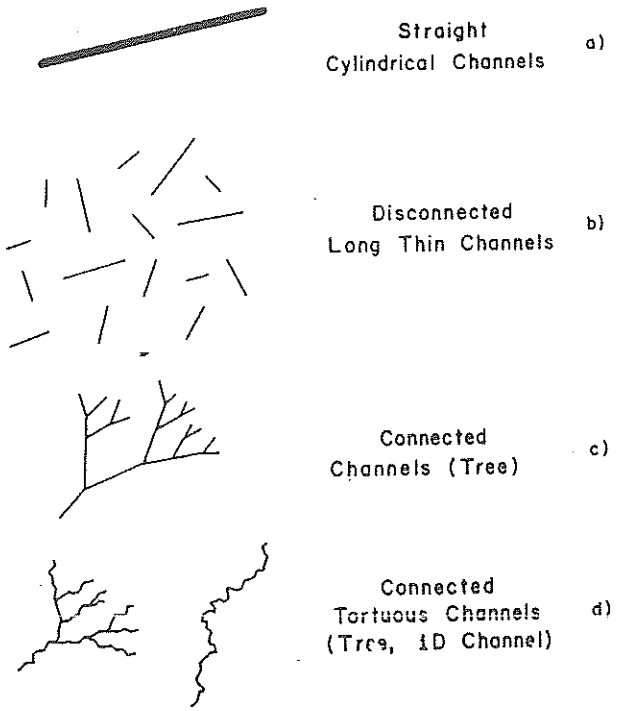

Figure 9: Summary of model lightning structures.

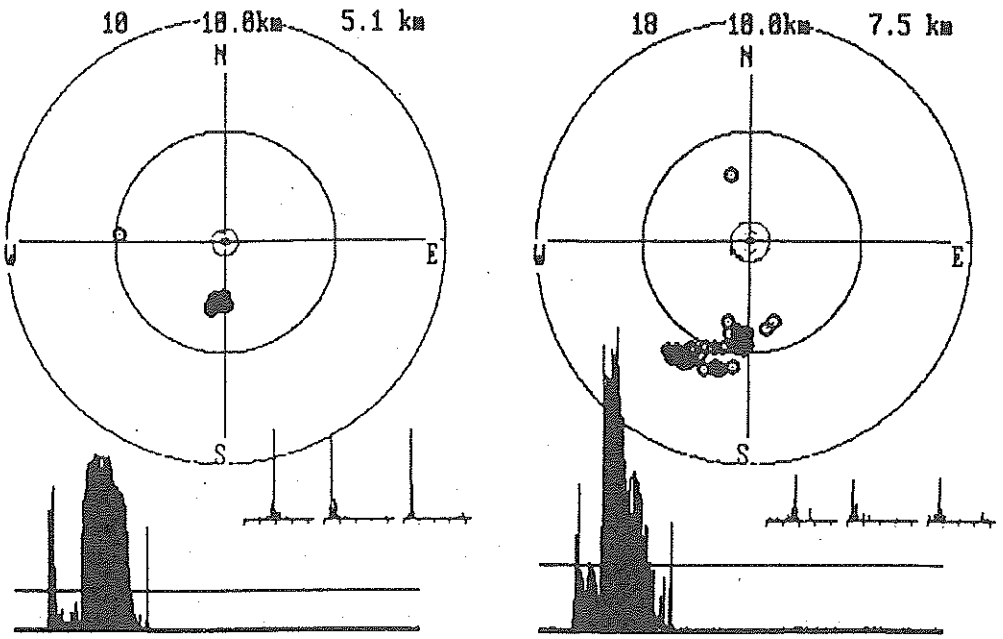

Figure 10: Polar plots of the positions, the amplitude variation (lower series) and phase distributions (0° to 360° in the 3 receiver channels) of lightning echoes in range gates 5.1 km (left) and 7.5 km (right) for a lightning stroke event 14:37:49 LT on 15 August 1995 over Chung-Li, Taiwan. The data points were separated by 4.8 ms. The small circles around each center point represent the horizontal cross section of the main antenna lobe.

So far there have been very few experiments utilizing MST radars for lightning observations [26, 14, 28, 47, 48]. Because of the transient and highly localized nature of lightning, care must be taken when designing an experiment. Clearly, coherent integration must be kept to a minimum. One should record the raw data to get the highest possible time resolution. Pulse coding (at least anything more than phase flipping every other pulse) is not a good idea. Also, the usual FFT method for obtaining Doppler information must be approached with caution. An episodic, non-periodic signal such as a lightning echo is not very amenable to an analysis technique that assumes periodicity. One should first examine the time-domain data (amplitude and phase), then decide how to proceed, perhaps with a wavelet method. Furthermore, lightning emits a broadband radio signal called sferics, which are very strong at VHF. Thus, every time there is a lightning discharge in the vicinity of the radar, the noise floor rises dramatically at all range gates. Finally, because of the high reflectivity at VHF, lightning echoes can enter through the antenna sidelobes. Thus, without interferometry one cannot be certain that the signal is coming from the main beam or a sidelobe. This last concern is highlighted in an interferometric observation of lightning events made with the Chung-Li VHF ST radar (Figure 10) [48]. Note that the lightning echo positions were well outside of the main beam. Although the system was not calibrated for absolute phase, the location of non-lightning echoes within the main lobe (not displayed here) showed that the lightning was really outside the main beam.

In the other project using MST radars for lightning observations, multiple frequencies were utilized at the Arecibo Observatory. In addition to the on-site 47- and 430-MHz radars, a 915-MHz boundary-layer radar was brought in for the campaign. An example of Doppler spectra with and without lightning is shown in Figure 11 [28]. Note the slightly upward motion of the ambient air seen in the VHF spectrum in (b), whereas only precipitation echoes are seen in the 430- and 915-MHz radars without lightning. The fact that the lightning spectra at all three frequencies match this air motion in this instance supports the idea that the plasma created by lightning drifts along with the air motion. However, in other instances the lightning spectral peak was shifted away from the ambient air peak. (Note also that the author attributes the apparent widening of the VHF spectrum with lightning to an artifact of the FFT processing.) Keener also prepared a scatter plot comparing the lightning channel Doppler velocities measured with the 430-MHz radar to the

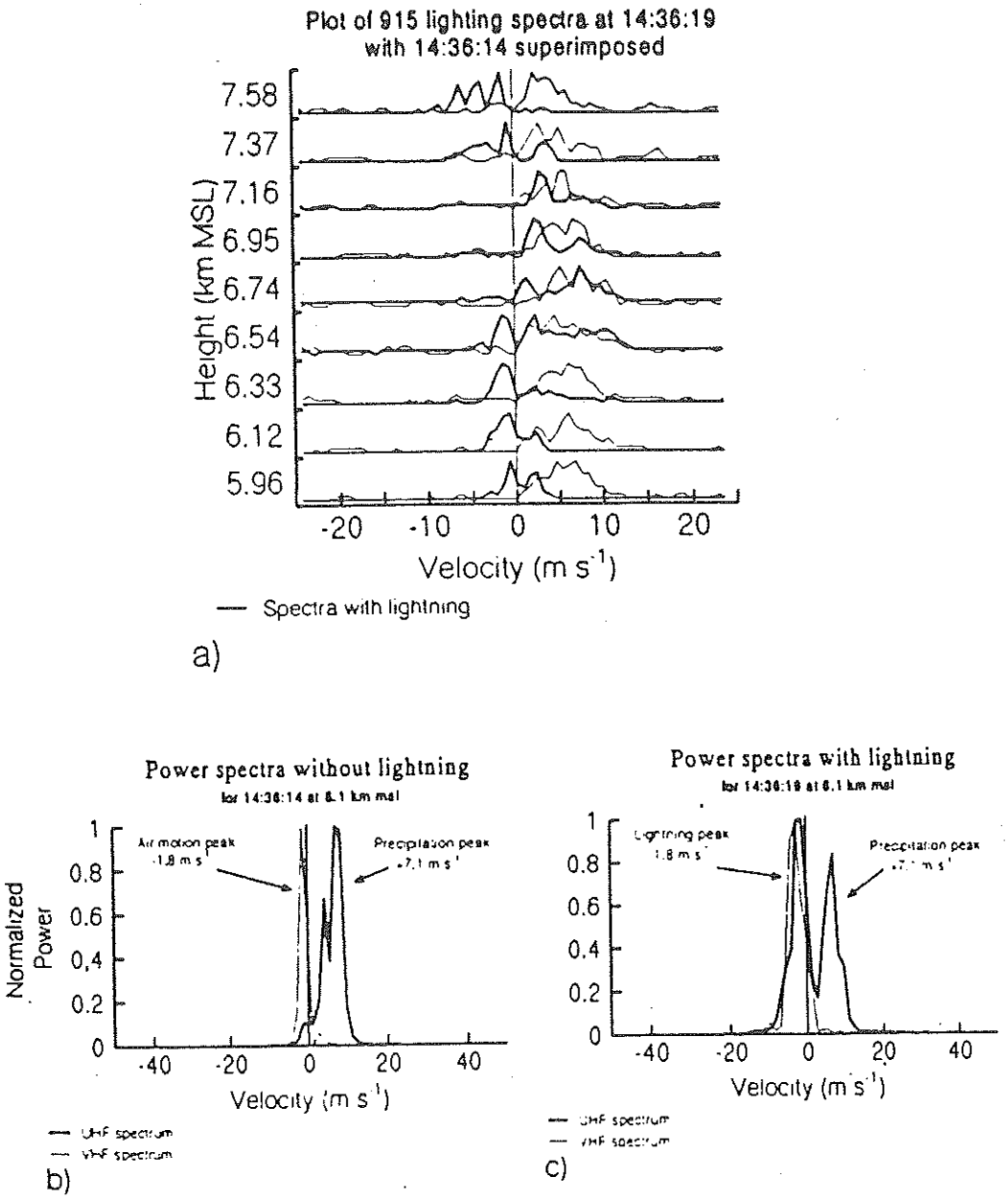

Figure 11: (a) Doppler spectra from the 915-MHz radar right before a lightning event (light line) and during (heavy line). (b) Doppler spectra at 6.1 km in height from the 47-MHz radar (light line) and the 430-MHz radar (heavy line) right before the same lightning event. (c) Same as (b) except during the lightning event. All radars were pointed vertically, with coaxial beams for the 47-MHz and 430-MHz radars and the 915-MHz radar located about 340 m away from the others. Negative velocity is upward, positive is downward.

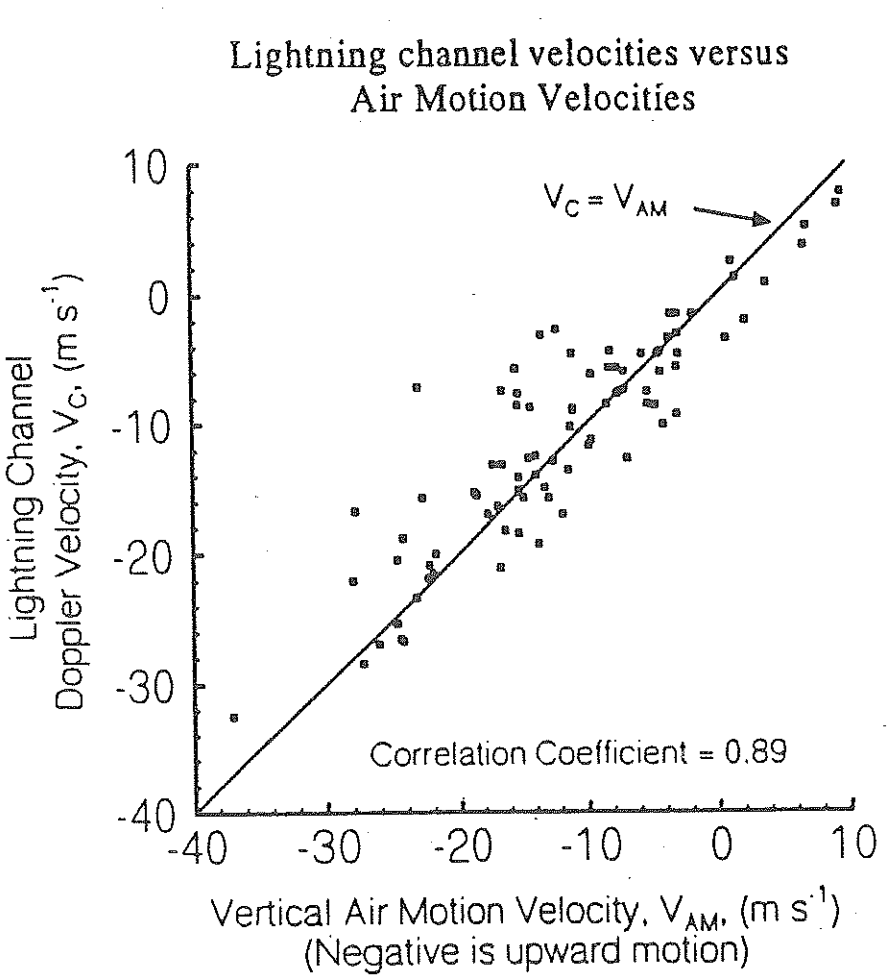

Figure 12: Lightning channel vertical Doppler velocities (430 MHz) versus air vertical velocity (47 MHz). The line is at 45°, corresponding to the case where the two velocities are equal. The correlation coefficient was 0.89.

air velocity observed with the 47-MHz radar (Figure 12 [28]). The correlation between the two quantities is not bad. Without interferometry to make sure that the lightning echo was coming from the main beam, some amount of scatter in this plot is to be expected. Since horizontal motions are generally much faster than vertical motions, even small angles off the vertical would project a false apparent velocity. With the recent addition of 430-MHz interferometric receiving antennas at Arecibo [43] such a discrimination should be possible.

Another reason for the difference between lightning plasma velocity and air velocity may be acceleration due to buoyancy and the Lorentz force. (And acceleration of the lightning channel *is* a common feature in Doppler radar observations.) A heated volume of air wants to rise, and an electrically charged particle streaming through a magnetic field wants to bend. One can perform simple calculations to estimate the importance of each effect. Assuming the lightning plasma channel to be a straight vertical cylinder with radius r (m), we can balance the buoyancy force (N)

$$F_b = \pi g(\rho - \rho_l)r^2 \tag{25}$$

where ρ_l (kg m^{-3}) is the density inside the lightning channel, to the drag force (N)

$$F_d = C_d \rho r w^2 \tag{26}$$

To get

$$w = \left(\frac{\pi g r}{C_d}\right) \tag{27}$$

for the equilibrium vertical velocity (m/s) if $\rho \gg \rho_l$. (C_d is estimated to be 0.9–1.2 [39].) Channels with a radius as large as 4 cm would get a shift upwards in velocity by about 1 m/s. However, buoyancy can only accelerate upwards, whereas observations show that the shift can also be downwards.

For the Lorentz force, we ignore the electric field term since a plasma is expected to maintain overall charge neutrality. Then the vertical acceleration due to a uniform current I (A) flowing inside a straight cylinder is

$$a_{vL} = \frac{\mu_0 H I}{\pi r^2 \rho_l} \sin\theta \cos\phi \tag{28}$$

where $\mu_0 = 1.26 \times 10^{-6}$ H/m is the free-space permeability, H (A/m) is the magnitude of the Earth's magnetic field, θ is the angle between the cylinder axis and the magnetic field, and ϕ is the angle between $I \times H$ and the vertical. With optimal geometry ($\theta = 90°$ and $\phi = 0°$) and reasonable numbers for the other parameters ($H = 55{,}000\gamma$, $r = 1$ cm, $\rho_l = 0.065$ kg m^{-3}, and $I = 20$ A), we get a_{vL} greater than 4 G, a significant force to be reckoned with. (This example was taken from [39].)

There are other interesting lightning effects on radar scatter. Increases in the precipitation Doppler spectra that last tens of milliseconds following a lightning event have been observed [40]. This has been attributed to refractive index inhomogeneities caused by lightning-produced shock waves. Polarization diversity radars have also observed the disorientation of high-altitude precipitation particles following lightning events [23], while a VHF radar has detected transient Doppler shifts of up to 300 m/s and a 6–7-Hz oscillation in velocity and amplitude of a scattering layer that support the idea that radars can detect lightning-generated acoustic waves [47]. However, the search by Doppler radar for the so-called rain gush phenomenon—the sudden increase in precipitation rate following lightning, which is believed to be caused by the cancellation of electrical levitation forces on charged particles by the lightning discharge—has yielded mostly negative results [68, 28].

So far all the experiments on radar lightning observations have lacked at least one of the following components: interferometry for channel mapping, VHF for unambiguous measurement of vertical air velocity, a higher frequency system for sensitivity to smaller precipitation particles, multiple beams or receivers for 3-D wind structure, and polarization diversity for particle type discrimination. If all of these instruments were deployed simultaneously to observe a common volume, we should be able to make great strides in the study of radar lightning echoes as well as the role of lightning and electrification in the development of thunderstorms.

2.2.1 Scattering From Sprites?

Anecdotal evidence of the upward discharge of lightning has abounded worldwide for over a century [54] (and even predicted on theoretical grounds [69, 70]), but proof of their existence was not obtained until 1989, when by chance a low-light TV camera recorded such an event [20]. Since then, what has come to be known as sprites [50] and elves [21], blue jets [66] and starters [65] have received intense scrutiny by experimentalists and theorists alike. So far the observations have been mainly in the optical band (Figure 13 shows a picture of a sprite [33]), but VLF electromagnetic waves have been shown to scatter from sprites [16] and are now used as a means for locating them [17]. As far as I know, there have not yet been any confirmed observations of sprites, elves, or jets with MST or incoherent-scatter radars (ISRs).

Although the optical phenomena have garnered the most attention from the mass media, other recently discovered lightning-related upward emission at other frequencies such as subionospherically propagating VLF signals [1], transionospheric VHF pulse pairs (TIPP) [27], and gamma-ray bursts [19] are also being investigated.

Figure 14 is a schematic of the various stratospheric and mesospheric effects of lightning and the proposed mechanisms for explaining them. The figure is taken from Pasko *et al.* [44], who give a good summary of the current thinking regarding sprites. The basic idea behind sprites is that the sudden redistribution of electric charge by lightning creates a quasi-electrostatic (QE) field above the thunderstorm, which induces current to flow and cause heating, ionization, and optical emission. The right charge configuration for this to occur is a positive cloud-to-ground (+CG) stroke, and observations show that sprites are exclusively related to +CG

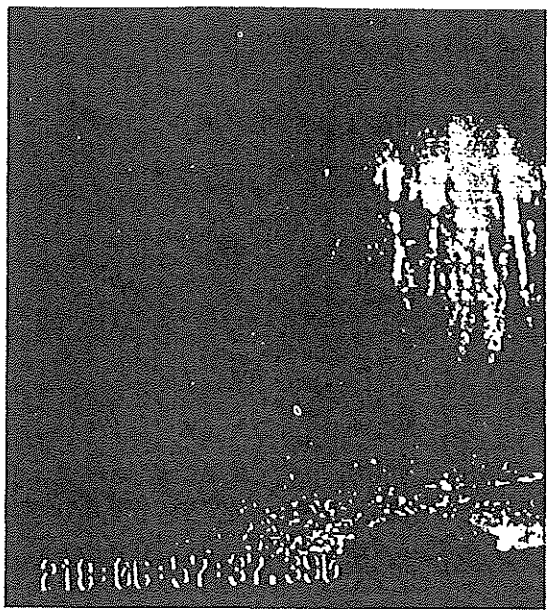

Figure 13: Sprite with a well-developed tendril structure at 6:57:37 UTC, 6 August 1994, associated with a positive cloud-to-ground flash with a 152-kA peak current that was located 330 km from the Yucca Ridge Field Station near Fort Collins, Colorado. The sprite top and base were estimated at 82 and 37 km. The sprite was visible to the naked eye. The cloud flash illuminates the horizon. The round object in the foreground is a satellite dish.

lightning. Other mechanisms such as electromagnetic pulses and runaway electron processes have also been proposed, and they may be important for the other phenomena such as elves, jets, and gamma-ray bursts.

Unlike the lightning strokes themselves, the QE-generated ionization is not expected to be overdense. In fact, model calculations show electron density enhancements in the mesosphere to be quite modest in absolute value (Figure 15 [44]), perhaps up to 1000 cm^{-3}. It may be possible for the most powerful ISRs to detect such an enhancement by either direct measurement of Thomson scatter or the indirect enhancement in turbulent scatter through the increase in electron density, N_e. Because the models are only at the stage of being able to reproduce the large-scale morphology of sprites and not the fine-scale features like the thin, vertical "tendrils" that extend throughout the mesosphere (much less anything at the 3-m Bragg scale of a VHF radar), we do not yet know whether there are likely to be inhomogeneities in N_e (and thus the refractive index) that might be a direct source of Bragg scattering for MST radars. Unambiguous detection may also be problematic, because with sprites we are likely dealing with very weak echoes in the midst of very strong scattering events (lightning) that could enter through antenna sidelobes and appear to come from much higher up than they are. But this is a wide-open field right now and the possibility of new discoveries using radars makes it very exciting.

2.3 Scattering From Meteors

As noted before, meteor observation by radar has had a history as long as radar itself, and until recently had been considered mature and "old hat" in many respects. The field seemed to have passed on a long time ago from the inquiry of basic issues to that of application and operational use. For atmospheric science, VHF meteor radars had proliferated around the globe for taking routine measurements of upper mesospheric winds. However, in the last few years unexpected results from the world's biggest VHF and UHF radars—Arecibo, Jicamarca, and EISCAT—have shown that we are still far from figuring out all there is to know about radar scattering from meteors.

But before we get into the latest reports, let me first step back and discuss the classical ideas of meteor

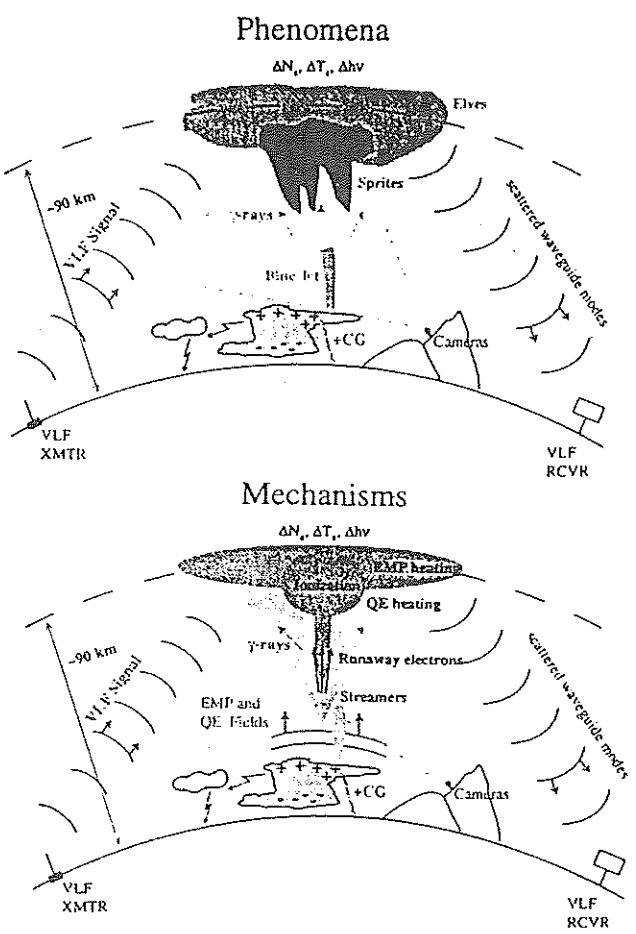

Figure 14: Illustration of different (top) phenomena and (bottom) theoretical mechanisms of lightning-ionosphere interactions operating at different altitudes and producing optical emissions ($\Delta\nu$) observed as sprites, blue jets, and elves, as well as heating (ΔT) and ionization changes (ΔN_e) detected as VLF signal changes.

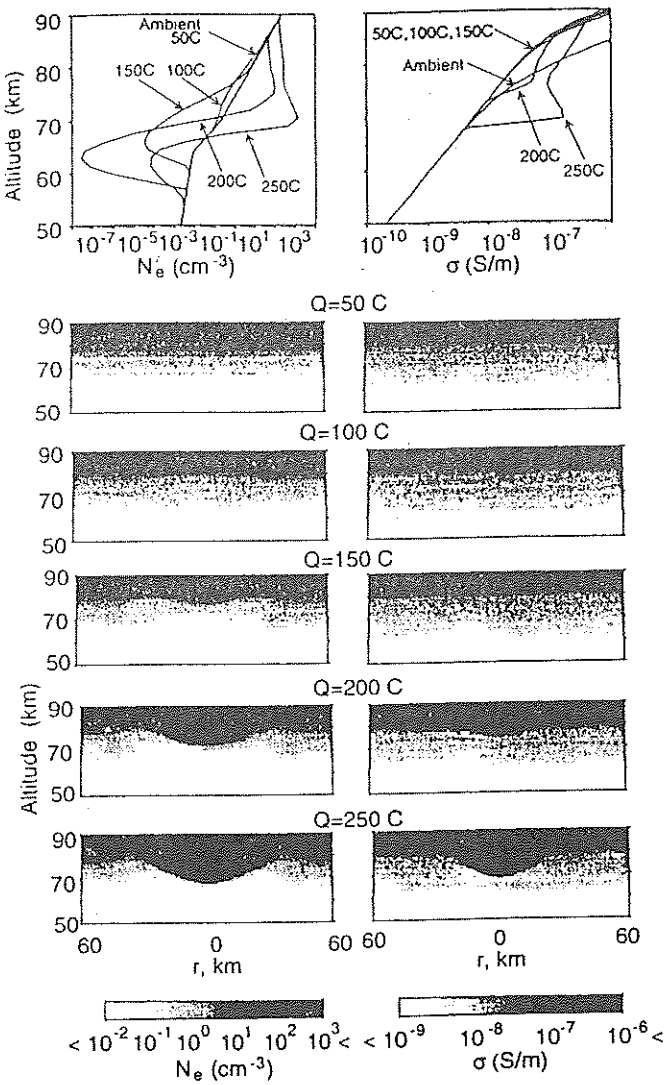

Figure 15: The altitude distribution of the electron density N_e and conductivity σ for different values of thundercloud charge Q at the moment of time $t = 1$ ms after the lightning discharge. r is the horizontal distance away from the lightning stroke. The top panels show altitude scans at $r = 0$.

radar scatter. The picture is that of a meteoroid shooting into the Earth's atmosphere and rapidly heating up the column of air through which it passes and ablates, leaving a cylinder of ionization as evidence of its passage. The trail terminates at the point where the meteoroid is completely vaporized. (If the meteoroid is not vaporized, then it falls to the Earth's surface as a meteorite.) The cylinder is initially straight and symmetric, with a radius that is mainly dependent on the air density, i.e., altitude—the lower the altitude, the smaller the radius, because the mean collisional distance is shorter. (These is also a dependence on the meteor velocity, which in turn is dependent on its orbital trajectory, but mostly the initial diameter is a function of altitude.) Then, diffusion causes the cylinder to expand, and other ambient dynamical processes like turbulence and shear deform the once-straight shape into a more convoluted form. All the while, recombination between positive species and electrons, and attachment of electrons to neutral particles (dust, for example), continue to drain away the enhancement in plasma density. Eventually, the trail disappears into the background.

Radar echoes are usually categorized as (1) coming from the head, i.e., spatially localized and moving along with the meteoroid, (2) reflecting from an overdense trail, or (3) scattering from an underdense trail. Let us first examine the trail echo.

Assuming that a cylindrical trail is created with an initial radius r_0 (m), the classical radial diffusion equation yields the solution for the electron density

$$N_e = \frac{q_l}{\pi\left(4D_e t + r_0^2\right)} e^{-\frac{r^2}{4D_e t + r_0^2}} \tag{29}$$

where D_e (m^2/s) is the electron diffusion coefficient, t (s) is time, and q_l (m^{-1}) is the electron line density (i.e., density per unit length). To find the critical radius r_c at which the nominal transition from overdense to underdense takes place, one can equate the critical electron density N_c given by (23) to (29) and get

$$r_c^2 = \left(4D_e t + r_0^2\right) \ln\left[\frac{r_e \lambda^2 q_l}{\pi^2\left(4D_e t + r_0^2\right)}\right] \tag{30}$$

where $r_e = e^2/4\pi\epsilon_0 m_e c^2 = 2.8 \times 10^{-15}$ m is the classical electron radius, and $c = 3 \times 10^8$ m/s is the speed of light. Note that if $r_e \lambda^2 q_l / \pi r_0^2 < 1$ then the trail will always be underdense. For an overdense condition, the scattering increases with the physical cross section, so we can differentiate (30) and equate the result to 0 to find the maximum r_c

$$r_{cm}^2 = \frac{r_e \lambda^2 q_l}{\pi^2 e} \tag{31}$$

where the e here is the base of the natural logarithm, not the electron charge. The equivalent echoing area of a long metallic column is $\pi R_0 r$ for spherical waves incident upon it from a source at a perpendicular distance R_0 [41], so the maximum radar cross section for an overdense trail is given by

$$\sigma_{od} = R_0 \lambda \left(\frac{r_e q_l}{e}\right)^{\frac{1}{2}} \tag{32}$$

To calculate the scattering cross section of an underdense trail, we need to perform a phase integral over the line of charge. One can conceptualize an effective length (m) defined by

$$L_e \equiv \left| \int_{-\infty}^{\infty} e^{-j\frac{4\pi}{\lambda}\left(R' - R_0\right)} dl \right| \tag{33}$$

where R' (m) is the distance of a line element dl from the radar. By making the approximation $R' - R_0 \approx l^2/(2R_0)$, we get a simple analytic expression

$$L_e = \left(\frac{R_0 \lambda}{2}\right)^{\frac{1}{2}} \tag{34}$$

Since the number of electrons within this effective length is $L_e q_l$, with the electric fields of the scattered waves from these electrons having the same phase, and the scattering cross section per electron is $4\pi r_e^2$, the underdense trail scattering cross section is given by

$$\sigma_{ud} = 2\pi R_0 \lambda r_e^2 q_l^2 \tag{35}$$

Note that overdense echoes are much less sensitive to changes in the line density than underdense echoes. Note also that the above results are for the trail perpendicular to the radar beam. Furthermore, for the underdense case it is assumed that the radius of the trail is much less than λ. Otherwise, the approximation of a line density breaks down, because different depths of the trail would experience different phases of the wave, thus creating an interference pattern in the scattered wave. For trail radii much longer than λ the radar cross section decreases steeply by an exponential factor $e^{-8\pi^2 r_0^2/\lambda^2}$. A useful formula for estimating the initial radius r_0 with respect to height is [34]

$$r_0 = 10^{0.075H - 7.9} \tag{36}$$

where the H (km) is the meteor height. (The formula was derived by estimating that the initial radius is of the order of 14 ionic mean-free-paths.) This means that underdense echoes will be hard to detect with a VHF radar above 110 km or so.

Head echoes have been harder to explain. The meteoroid itself is too small a physical target for Rayleigh scattering. A ball of ionization much larger than the meteroid has been suggested, but unlike trail echoes, head echoes have no appreciable duration, so it is hard to explain the near-instant disappearance of the ionization after the meteroid passage. Also what might create the ionization at a distance away from the meteroid is unknown. Shock waves and ultraviolet light have been suggested, but criticized on various grounds. I think we can safely state that there is no generally accepted explanation for head echoes at this time. The new observations from the big radars have not cleared up the picture, either.

Some data examples are in order at this point. Figure 16 shows a perpendicular trail echo (top panel) and a combination down-the-beam head and trail echo [72]. The smooth decay of echo power with time of the perpendicular trail indicates that it was a classical underdense trail. Such meteor events can be used to estimate the electron diffusivity by relating the measured e^{-2} decay time to the theoretical diffusion time constant (s)

$$\tau_d = \frac{\lambda^2}{16\pi^2 D_e}. \tag{37}$$

One can go further and try to extract the temperature fluctuations, which under the Boussinesq approximation is proportional to the diffusivity fluctuations [55]. However, the relationship between electron ambipolar diffusivity and the neutral gas parameters is not necessarily so straightforward, especially in the possible presence of charged meteoric dust particles [11, 10]. The presence of charged dust could bias the inferred temperature values [13]; indeed, such an effect might explain the discrepancy between lidar- and meteor-radar-inferred temperatures [8].

These well-behaved underdense trail echoes are also used to infer the background air motion, since they are presumed to simply drift along with the wind. This technique for wind measurement has been successfully applied to MST radars [3, 59], with refinements such as interferometry for unambiguous angle-of-arrival information (e.g., [42, 25]).

But while meteor radars with their wide beams had mainly detected perpendicular trail echoes, narrow-beam MST radars and wind profilers detect a much larger fraction of down-the-beam echoes. A classification of meteor echoes observed by a VHF wind profiler is shown in Figure 17 [60]. Under this classification scheme, the "clipped" and "noise spike" classes are instrument-caused rather than real meteoric types. "Multiple echoes" are just two or more unrelated events occurring over a short period of time, and "trail formation" means a head echo. Since the best wind estimation is derived from the underdense types, clearly the meteor echoes must be sorted out before analysis takes place. The classification statistics for this particular system are given in Figure 18 [60].

Down-the-beam events are useful for inferring the characteristics of the meteroid itself, and thus is of more interest to astronomers. Large MST radars and ISRs can contribute uniquely to this field due to their high sensitivity. For example, the Arecibo 430-MHz radar was recently used to discover a new class of sporadic micrometeors estimated to be of the order of 1 μg in mass and 15th magnitude in brightness [37].

It is still a mystery why the ratio of down-the-beam to perpendicular meteor echoes is so much higher for MST/ISR systems than for the traditional VHF meteor radars. Simple geometric considerations of the antenna beam cannot explain it, since both types should be sampled equally less for a narrower-beam radar. At first it was thought that the higher power of the MST radar made head echoes more "visible," but recent results show that even the low-power wind profilers detect more head echoes than do meteor radars.

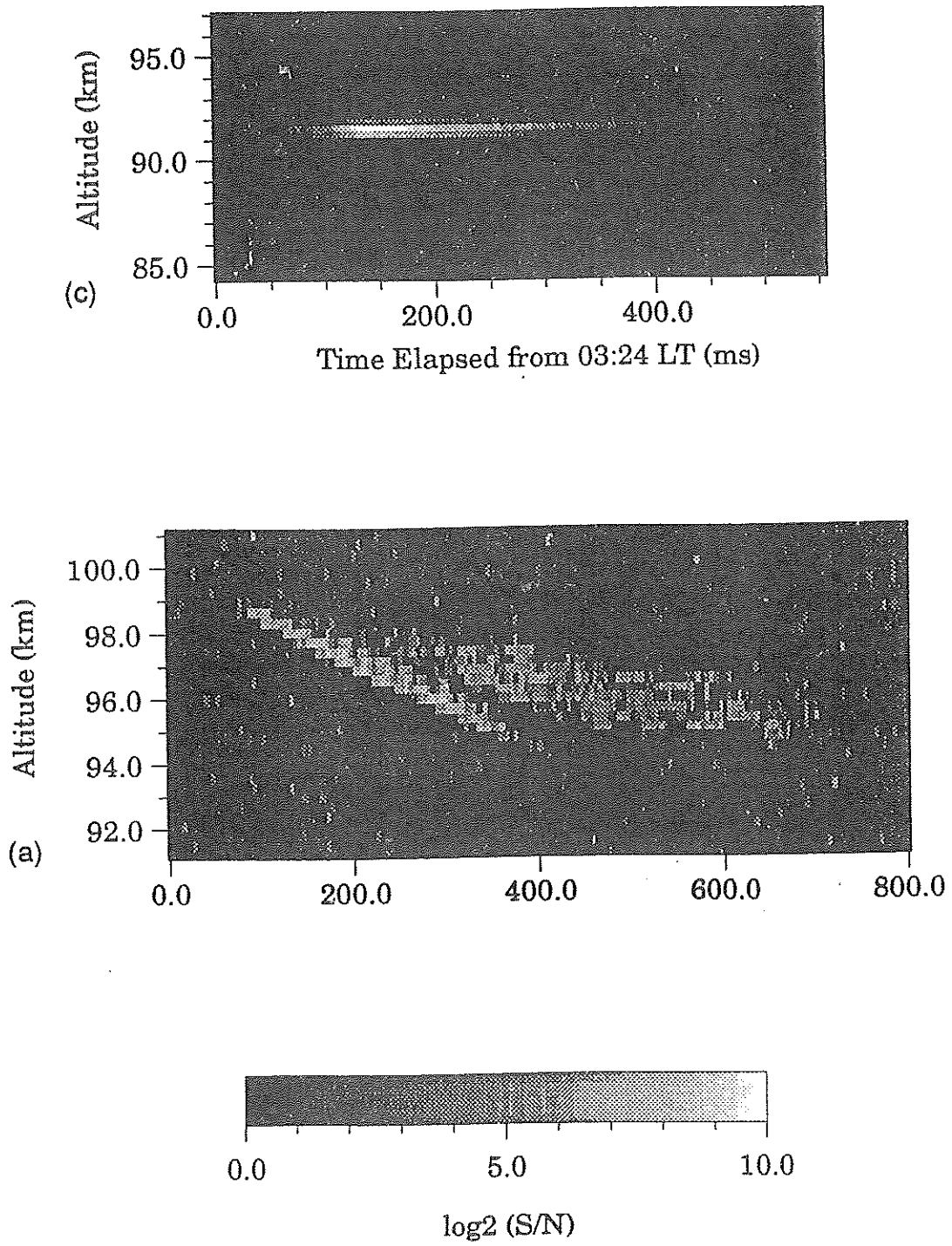

Figure 16: An example of a classic underdense trail perpendicular to the radar beam (top) and a combination head and trail echo (bottom) observed with the Arecibo 47-MHz radar.

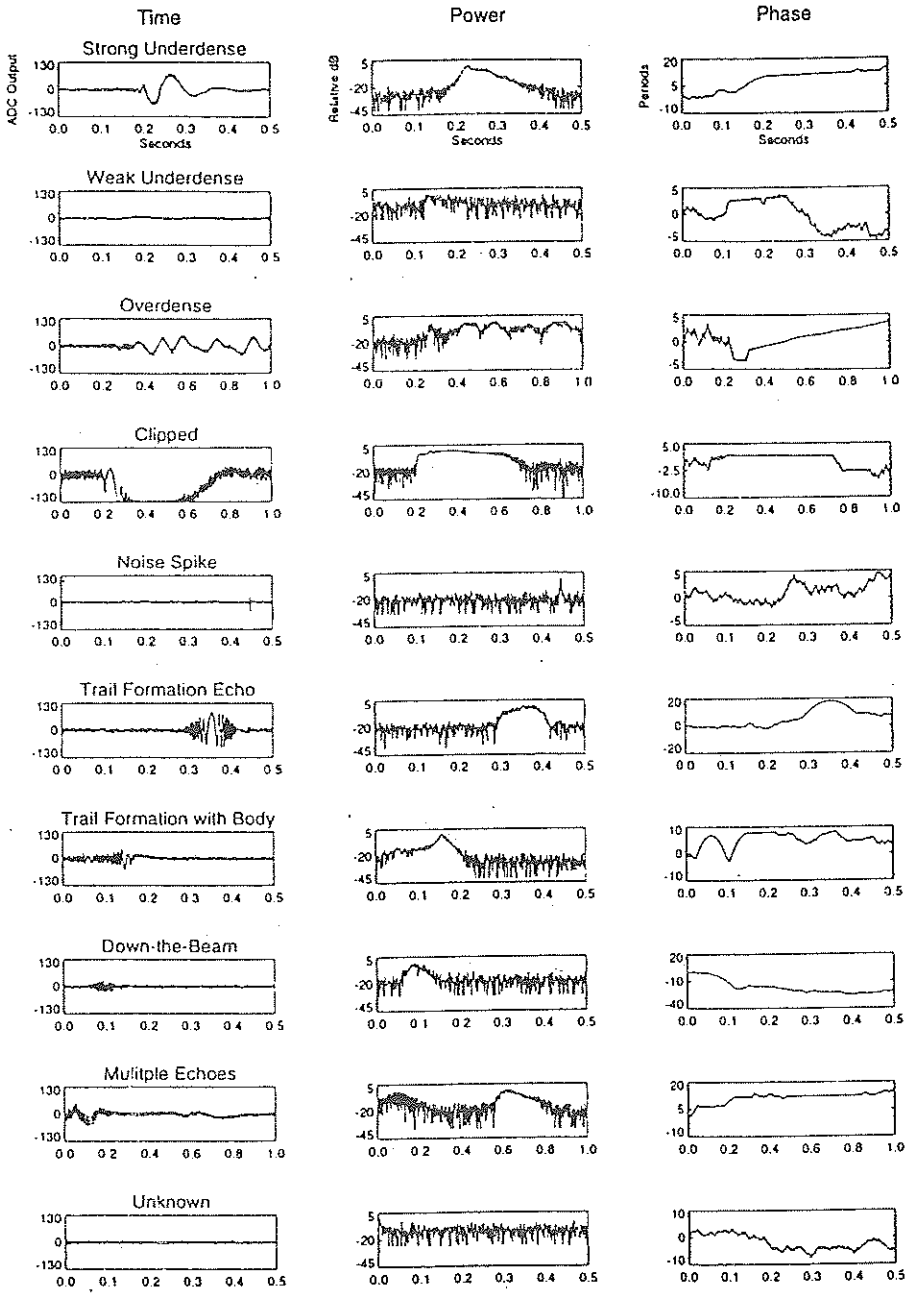

Figure 17: Examples of voltage, power, and phase versus time plots of each of the different meteor signal classes as observed with the MEDAC/Buckland Park VHF radar.

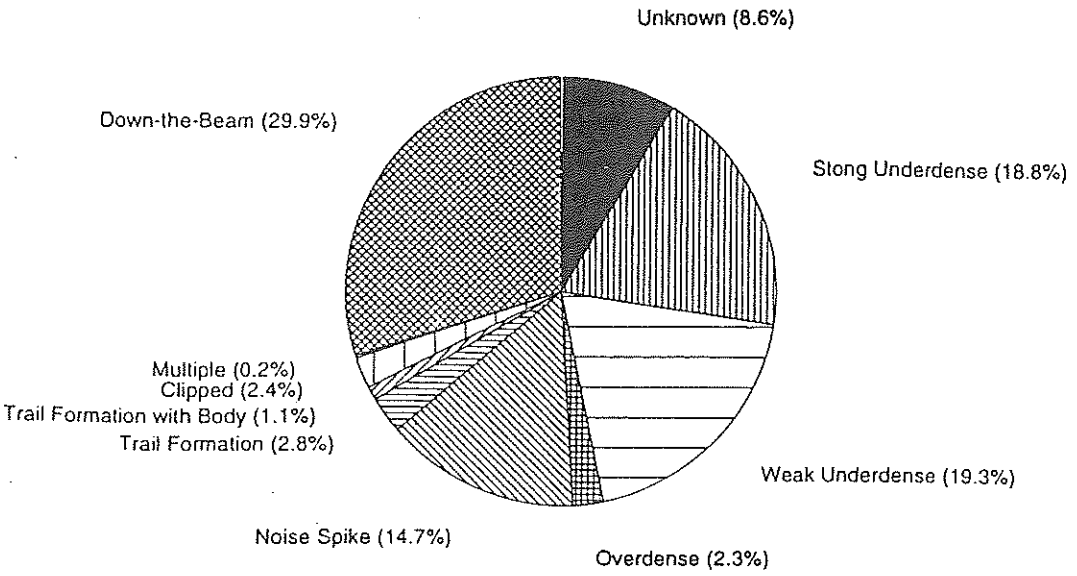

Figure 18: Distribution of meteor echo classes from the MEDAC/Buckland Park data set.

Another puzzle is the time gap between the head echo and its corresponding trail echo (Figure 16, bottom). In this case, as the meteoroid was traveling down the beam, the trail could not have been perpendicular. The trail also does not exhibit a smooth decay with time. Therefore, it cannot be a classic perpendicular underdense trail. Perhaps it was a trail that was deformed by turbulence and wind shear so that parts of the "cylinder" surface became momentarily perpendicular to the radar beam. (This idea is known as the "glint" theory.) However, it seems implausible that such deformation could have taken place within tens of milliseconds as is necessary to explain the observation.

Down-the-beam head echoes are also much more prevalent for UHF ISRs [46, 73, 71]. Simultaneous UHF/VHF observations have yielded very different wavelength dependences of the head echo scattering cross section. The EISCAT results show higher cross sections at shorter wavelengths (like Rayleigh scattering) [64], while the Arecibo results indicate higher cross sections at longer wavelengths. This is a very fundamental disagreement that is currently under investigation.

At the magnetic equator, the Jicamarca VHF radar has been used to observe long duration (2 s to 3 minutes) meteor echoes whose Doppler spectral skewness is clearly correlated with the direction of the E-region zonal electric field [7, 6]. Figure 19 shows the power map (top) and the Doppler spectral skewness (bottom) of the equatorial electrojet (cloud-like echoes near the top of the plots) and meteors (vertical streaks) [6]. Note that the Doppler spectral skewness of the meteor echoes reverses sign when the electrojet is not present (i.e., when the electrojet electric field reverses direction from westward to eastward), indicating the dependence of the meteor scattering process on plasma electrodynamics. The investigators have concluded that meteor trails deposited within the equatorial electrojet must carry intense discharge currents that excite two-stream and/or gradient-drift instabilities. The direction of electron motion responsible for the discharge current then agrees with the Doppler shift of the high frequency components in the meteor echoes.

Finally, in an incredibly fortuitous coincidence, a sounding rocket with an electron density probe happened to fly through a meteor trail that was simultaneously detected with the Poker Flat MST radar [29]. The trail as measured by the rocket was at 92 km in altitude, 42 m thick with a peak electron density of 40,000 cm^{-3}, which was 50% above the ambient density, and the edges were extremely sharp with an e-folding length of 1.2 m. A Fourier analysis of the density fluctuations inside the trail showed a turbulence-like spectrum that extended down through the 3-m Bragg scale of the radar, while a wavelet scalogram also showed that the edge gradients also had considerable power at the Bragg scale. The radar echo persisted for several cycles of the radar Doppler beam swinging, had a downward Doppler velocity of about 4 m/s and a spectral width of about 6 m/s. The low electron density ruled out overdense echoing, while the thickness of the trail ruled out classic underdense scattering. The authors proposed that a charged-dust mechanism for lowering

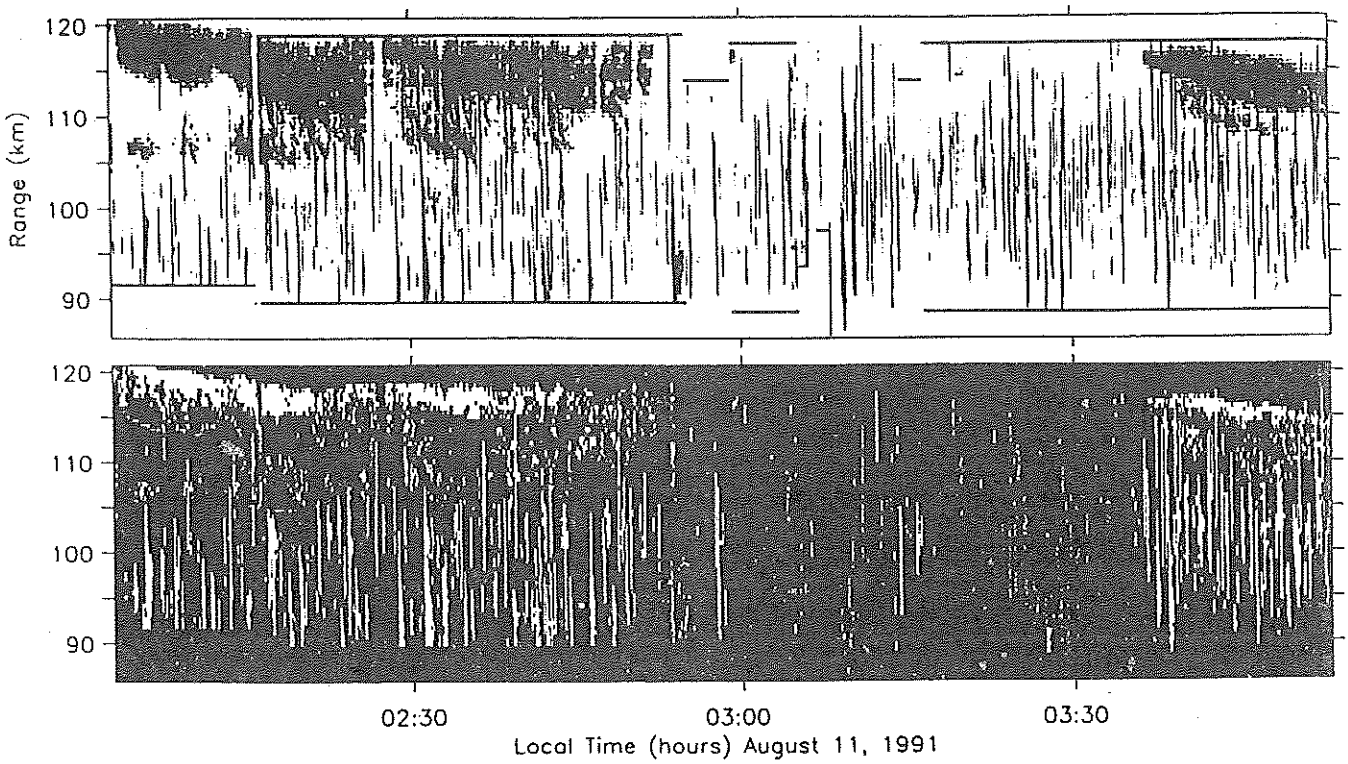

Figure 19: (Top) intensity and (bottom) Doppler spectral skewness maps of Jicamarca backscatter data observed on 11 August 1991. For the skewness data, white is negative (away from radar) and black is positive (towards radar).

the electron diffusivity analogous to PMSE (see Section 3), was responsible for the maintenance of electron density structures at such small scales. In a companion paper, a technique for the detection of such charged meteoric dust using an ISR was outlined [13].

In summary, meteor radar research is far from dead. As we have seen, there are fundamental problems that need to be solved. And MST/ISR systems have been instrumental in bringing about a renaissance to the field. Furthermore, in the next several years the annual Leonid meteor shower is expected to reach a peak in activity, and the optimal location for observation of the 1998 shower is in the central Asian sector (Table 1 [36]). Plans should be laid ahead of time for radar observations of these events.

3 Scattering From Dusty/Icy Plasma: Polar Mesosphere Summer Echoes

See the review paper by Cho and Rottger [12]

4 Coherent Scattering From F-region Plasma: Equatorial Spread F

See the relevant section in a book by Fejer [18]

Table 1: Observational circumstances for predicted Leonid maxima (1995-2002)

Earth at longitude of descending node Date	Time (hrs UT)	Solar longitude (2000.0)	(R_C-R_E) (AU)	Days before/ after comet's nodal passage*	Age of Moon (days)	Optimum location for observation**	Circumstances in the UK	Possible Leonid activity
1995 Nov 18	00.1	$235^0.24$	-0.00985	-837. 82	24.8	Middle East; Eastern Europe	Dark; radiant low	Possible enhanced activity. ~50 -100m/h
1996 Nov 17	06.5	$235^0.25$	-0.00867	-472.52	6.2	North Atlantic; Eastern Canada & USA	Dawn twilight; radiant high	Good chance of a significant shower. ~150 -300 m/h; little chance of a storm
1997 Nov 17	13.2	$235^0.27$	-0.00796	-107.28	17.1	North Pacific	Day light	Very good chance of an outstanding shower; possible storm. ~1000m/h
1998 Nov 17	19.8	$235^0.29$	-0.00841	+258.01	28.0	Eastern & Central Asia	Dark; radiant below horizon	Very good chance of an outstanding shower; possible storm. ~5000m/h
1999 Nov 18	01.6	$235^0.28$	-0.00714	+623.36	9.3	Eastern & Central Europe	Dark; radiant fairly low	Very good chance of an outstanding shower; probable storm. ~5000m/h
2000 Nov 17	07.8	$235^0.28$	-0.00534	+988.63	20.2	Eastern & Central Canada & USA	Dawn; radiant high	Very good chance of an outstanding shower; possible storm. ≅ 1000m/h
2001 Nov 17	14.4	$235^0.30$	-0.00492	+1353.56	1.6	North Pacific	Daylight	Good chance of a significant shower. ~150 -300m/h; little chance of a storm
2002 Nov 17	21.6	$235^0.34$	-0.00637	+1718.17	12.5	Central & Western Asia; Middle East	Dark; radiant below horizon	Probable enhanced activity. ~50 -100m/h

* Comet 55P/Tempel - Tuttle is computed to pass through the descending node of its orbit on 1998 March 4.

** 'Optimum location for observation' is the region on the Earth's surface in the northern hemisphere where the Leonid radiant is well placed in a dark sky at the time the Earth reaches the ecliptic longitude of the comet's descending node.

References

[1] W. C. Armstrong. Recent advances from studies of the Trimpi effect. *Antarc. J.*, 18:281, 1983.

[2] D. Atlas, editor. *Radar in Meteorology*. 806 pp., American Meteorological Society, Boston, 1990.

[3] S. K. Avery, A. Riddle, and H. Balsley. Poker Flat, Alaska MST radar as a meteor radar. *Radio Sci.*, 18:1021-1027, 1983.

[4] L. J. Battan. *Radar Observation of the Atmosphere*. pp. 324, Univ. of Chicago Press, Chicago, 1973.

[5] K. V. Beard. Simple altitude adjustments to raindrop velocities for Doppler radar analysis. *J. Atmos. Oceanic Technol.*, 2:468 471, 1985.

[6] E. Chapin and E. Kudeki. Plasma wave excitation on meteor trails in the equatorial electrojet. *Geophys. Res. Lett.*, 21:2433 2436, 1994.

[7] E. Chapin and E. Kudeki. Radar interferometric imaging studies of long-duration meteor echoes observed at Jicamarca. *J. Geophys. Res.*, 99:8937 8949, 1994.

[8] P. B. Chilson, P. Czechowsky, and G. Schmidt. A comparison of ambipolar diffusion coefficients in meteor trains using VHF radar and UV lidar. *Geophys. Res. Lett.*, 23:2745 2748, 1996.

[9] P. B. Chilson, C. W. Ulbrich, M. F. Larsen, P. Perillat, and J. E. Keener. Observations of a tropical thunderstorm using a vertically pointing, dual-frequency, collinear beam Doppler radar. *J. Atmos. Oceanic Tech.*, 10:663 673, 1993.

[10] J. Y. N. Cho, C. M. Alcala, M. C. Kelley, and W. E. Swartz. Further effects of charged aerosols on summer mesospheric radar scatter. *J. Atmos. Terr. Phys.*, 58:661 672, 1996.

[11] J. Y. N. Cho, T. M. Hall, and M. C. Kelley. On the role of charged aerosols in polar mesosphere summer echoes. *J. Geophys. Res.*, 97:875 886, 1992.

[12] J. Y. N. Cho and J. Rottger. An updated review of polar mesosphere summer echoes: Observation, theory, and their relationship to noctilucent clouds and subvisible aerosols. *J. Geophys. Res.*, 102:2001 - 2020, 1997.

[13] J. Y. N. Cho, M. P. Sulzer, and M. C. Kelley. Meteoric dust effects on D-region incoherent scatter radar spectra. *J. Atmos. Solar Terr. Phys.*, 1998. in press.

[14] T. S. Dennis. *Analysis of VHF Doppler radar observations of a tropical thunderstorm*. PhD thesis, Clemson Univ., Clemson, S.C., 150 pp., 1990.

[15] R. J. Doviak and D. S. Zrnic. *Doppler Radar and Weather Observations.* 562 pp., Academic Press, San Diego, 2nd edition, 1993.

[16] R. L. Dowden, J. B. Brundell, and W. A. Lyons. Are VLF RORDs and optical sprites produced by the same cloud-to-ionosphere discharge? *J. Geophys. Res.*, 101:19,175 19,183, 1996.

[17] R. L. Dowden, J. B. Brundell, W. A. Lyons, and T. Nelson. Detection and location of red sprites by VLF scattering of subionospheric transmissions. *Geophys. Res. Lett.*, 23:1737 1740, 1996.

[18] B. G. Fejer. Natural ionospheric plasma waves. in *Modern Ionospheric Science*, edited by R. Ruster and K. Schlegel, pp. 216 273, European Geophysical Society, Katlenburg-Lindau, Germany, 1996.

[19] G. J. Fishman, P. N. Bhat, and R. Mallozzi. Discovery of intense gamma-ray Hashes of atmospheric origin. *Science*, 264:1313, 1994.

[20] R. C. Franz, R. J. Nemzek, and J. R. Winckler. Television image of a large upward electrical discharge above a thunderstorm system. *Science*, 249:48 51, 1990.

[21] H. Fukunishi, Y. Takahashi, M. Kubota, K. Sakanoi, U. S. Inan, and XV. A. Lyons. Lightning-induced transient luminous events in the lower ionosphere. *Geophys. Res. Lett.*, 23:2157 2160, 1996.

[22] R. Gunn and G. D. Kinzer. The terminal velocity of fall for water droplets in stagnant air. *J. Meteorol.*, 6."24.'3-248, 1949.

[23] A. Hendry and G. C. McCormick. Radar observations of the alignment of precipitation particles by electrostatic fields in thunderstorms. *J. Geophys. Res.*, 81:5353 5357, 1976.

[24] W. K. Hocking. Measurement of turbulent energy dissipation rates in the middle atmosphere by radar techniques: A review. *Radio Sci.*, 20:1403 1422, 1985.

[25] W. K. Hocking and T. Thayaparan. Simultaneous and colocated observation of winds and tides by MF and meteor radars over London, Canada. (43°N, 81°W), during 1994 1996. *Radio Sci.*, 32:833 865, 1997.

[26] D. N. Holden. *Radar observations of changes in precipitation size spectra associated with lightning*. PhD thesis, Clemson Univ., Clemson, S.C., 93 pp., 1987.

[27] D. N. Holden, C. P. Munson, and J. C. Devenport. Satellite observations of transionospheric pulse pairs. *Geophys. Res. Lett.*, 22:889 892, 1995.

[28] J. E. Keener. *A Study of Lightning, Dynamics, and Microphysics in a Tropical Thunderstorm Using UHF and VHF Doppler Radars*. PhD thesis, Clemson Univ., Clemson, S.C., 125 pp., 1995.

[29] M. C. Kelley, C. M. Alcala, and J. Y. N. Cho. Detection of a meteor contrail and meteoric dust in the Earth's upper mesosphere. *J. Atmos. Solar Terr. Phys.*, 1998. in press.

[30] M. F. Larsen and J. Rottger. Observations of thunderstorm reflectivities and Doppler velocities measured at VHF and UHF. *J. Atmos. Oceanic Technol.*, 4:151 159, 1987.

[31] J. O. Laws and D. A. Parsons. The relationship of raindrop size to intensity. *Trans. AGU*, 24:452 460, 1943.

[32] M. G. H. Ligda. The radar observation of lightning. *J. Atmos. Terr. Phys.*, 9:329 346, 1956.

[33] W. A. Lyons. Sprite observations above the U.S. High Plains in relation to their parent thunderstorm systems. *J. Geophys. Res.*, 101:29,641 29,652, 1996.

[34] L. A. Manning. The initial radius of meteoric ionization. *J. Geophys. Res.*, 63:181 196, 1958.

[35] J. S. Marshall, W. Hitschfeld, and K. L. S. Gunn. Advances in radar weather. *Adv. Geophys.*, 2:1 56, 1955.

[36] J. W. Mason. The Leonid meteors and comet 55P/Temple-Tuttle. *J. Brit. Astron. Assoc.*, 105:219 235, 1905.

[37] J. D. Mathews, D. D. Meisel, K. P. Hunter, V. S. Getman, and Q. Zhou. Very high resolution studies of micrometeors using the Arecibo 430 MHz radar. *Icarus*, 126:157 169, 1997.

[38] R. J. Matson and A. W. Huggins. The direct measurement of the sizes, shapes, and kinematics of falling hailstones. *J. Atmos. Sci.*, 37:1107 1125, 1980.

[39] V. Mazur, D. S. Zrnic, and W. D. Rust. Lightning channel properties determined with a vertically pointing Doppler radar. *J. Geophys. Res.*, 90:6165 6174, 1985.

[40] V. Mazur, D. S. Zrnic, and WV. D. Rust. Transient changes in Doppler spectra of precipitation associated with lightning. *J. Geophys. Res.*, 92:6699 6704, 1987.

[41] D. XV. R. McKinley. *Meteor Science and Engineering*. McGraw-Hill, New York, 1961.

[42] T. Nakamura, T. Tsuda, M. Tsutsumi, K. Kita, T. Uehara., S. Kato, and S. Fukao. Meteor wind observations with the MU radar. *Radio Sci.*, 26;857 869, 1991.

[43] R. D. Palmer, M. F. Larsen, P. B. Howell, J. Y. N. Cho, R. M. Narayanan, and M. C. Kelley. A new spatial interferometry capability using the Arecibo 430-MHz radar. *Radio Sci.*, 32:749 755, 1997.

[44] V. P. Pasko, U. S. Inan, T. F. Bell, and Y. N. Taranenko. Sprites produced by quasi-electrostatic heating and ionization in the lower ionosphere. *J. Geophys. Res.*, 102:4529 4561, 1997.

[45] J. L. Pawsey. Radar observations of lightning on 1.5 meters. *J. Atmos. Terr. Phys.*, 11:289 - 290, 1957.

[46] A. Pellinen-Wannberg and G. Wannberg . Meteor observations with the European incoherent scatter UHF radar. *J. Geophys. Res.*, 99:11,379 11,390, 1994.

[47] J. Rottger, C. H. Liu, C. J. Pan, and S. Y. Su. Characteristics of lightning echoes observed with VHF ST radar. *Radio Sci.*, 30:1085 1097, 1995.

[48] J. Rottger, C.-J. Pan, C.-H. Liu, S.-Y. Su, and J. Wu. VHF radar interferometer observations of lightning echoes and tropospheric scattering centers. in *Solar-Terrestrial Energy Program: Proceedings of the Seventh Workshop on Technical and Scientific Aspects of MST Radar*, pp. 368-371, SCOSTEP Secretariat, Boulder, Colo., 1996.

[49] J. P. Schafer and W. M. Goodall. Observations of the Kennelly-Heaviside layer heights during the Leonid meteor shower of Nov. 1931. *Proc. Inst. Radio Eng.*, 20:1941 1945, 1932.

[50] D. D. Sentman, E. M. Wescott, D. L. Osborne, D. L. Hampton, and M. J. Heavner. Preliminary results from the Sprites 94 campaign: Red sprites. *Geophys. Res. Lett.*, 22:1205 1208, 1995.

[51] H. Shono. Reflection of microwaves accompanying lightning. *Rep. Inst. Sci. Technol.*, 1:184 190, 1947.

[52] A. M. Skellett. The effect of meteors on radio transmission through the Kennelly-Heaviside layer. *Phys. Rev.*, 37:1668, 1931.

[53] D. M. Swingle. A new use for weather radar. *Trans. New York Academy of Sciences*, 20:348 352, 1958.

[54] H. Toynbee and T. Mackenzie. Notice. *Nature*, 33:245, 1886.

[55] AI. Tsutsumi, T. Tsuda, T. Nakamura, and S. Fukao. Temperature fluctuations near the mesopause inferred from meteor observations with the middle and upper atmosphere radar. *Radio Sci.*, 29:599 610, 1994.

[56] C. W. Ulbrich. Natural variations in the analytical form of the raindrop-size distribution. *J. Climate Appl. Meteorol.*, 22:1764 1775, 1983.

[57] Ail. A. Uman. *Lightning*. 264 pp., McGraw Hill, New York, 1969.

[58] M. A. Uman. *The Lightning Discharge*. 377 pp., Academic Press, San Diego, 1987.

[59] T. A. Valentic, J. P. Avery, and S. K. Avery. MEDAC/SC: A third generation meteor echo detection and collection system. *IEEE Trans. Geosci. Remote Sens.*, 34:15 21, 1996.

[60] T. A. Valentic, J. P. Avery, S. K. Avery, M. A. Cervera, W. G. Elford, R. A. Vincent, and I. M. Reid. A comparison of meteor radar systems at Buckland Park. *Radio Sci.*, 31:1313 1329, 1996.

[61] K. Wakasugi, B. B. Balsley, and T. L. Clark. The VHF Doppler radar as a tool for cloud and precipitation studies. *J. Atmos. Oceanic Technol.*, 4:27.'3 280, 1987.

[62] K. Wakasugi, A. Mizutani, and 51. M. Matsuo. A direct method for deriving drop-size distribution and vertical air velocities from VI-IF Doppler radar spectra. *J. Atmos. Oceanic Technol.*, 3:623 629, 1986.

[63] K. Wakasugi, A. Mizutani, M. Matsuo, S. Fukao, and S. Kato. Further discussion on deriving drop-size distribution and vertical air velocities directly from VHF Doppler radar spectra. *J. Atmos. Oceanic Technol.*, 4:170 179, 1987.

[64] G. Wannberg, A. Pellinen-Wannberg, and A. Westman. An ambiguity-function-based method for analysis of Doppler decompressed radar signals applied to EISCAT measurements of oblique UHF-VHF rneteor studies. *Radio Sci.*, 31:497 518, 1996.

[65] E. M. Wescott, D. D. Sentman, M. J. Heavner, D. L. Hampton, D. L. Osborne, and O. H. Vaughan, Jr. Blue starters: Brief upward discharges from an intense Arkansas thunderstorm. *Geophys. Res. Lett.*, 23:2153 - 2156, 1996.

[66] E. M. Wescott, D. D. Sentman, D. Osborne, D. Hampton, and M Heavner. Preliminary results from the Sprites94 aircraft campaign. 2: Blue jets. *Geophys. Res. Lett.*, 22:1209 1212, 1995.

[67] E. R. Williams, S. G. Geotis, and A. B. Bhattacharya. A radar study of the plasma and geometry of lightning. *J. Atmos. Sci.*, 46:117'3 1185, 1989.

[68] E. R. Williams and R. Lhermitte. Radar tests of the precipitation hypothesis for thunderstorm electrification. *J. Geophys. Res.*, 88:10,984 10,992, 1983.

[69] C. T. R. Wilson. The electric field of a thundercloud and some of its effects. *Proc. Phys. Soc. London*, 37:32D, 1925.

[70] C. T. R. Wilson. A theory of thundercloud electricity. *Proc. B. Soc. London Ser. A*, 236:297, 1956.

[71] Q. H. Zhou and M. C. Kelley. Meteor observation by the Arecibo 430 MHz ISR II. Results from time-resolved observations. *J. Atmos. Solar Terr. Phys.*, 59:739 752, 1997.

[72] Q. H. Zhou, P. Perillat, J. Y. N. Cho, and J. D. Mathews. Simultaneous meteor echo observations by large aperture VHF and UHF radars. *Radio Sci.*, 1998. submitted.

[73] Q. H. Zhou, C. A. Tepley, and 5'1. P. Sulzer. Meteor observation by the Arecibo 4:30 MHz ISR I. Results from time-integrated observations. *J. Atmos. Terr. Phys.*, 57:421 431, 1995.